Progress In Electromagnetics Research C, Vol. 171, 501–514, 2026

PIER C

(Received 21 May 2026, Accepted 18 June 2026, Scheduled 20 July 2026)

A Fixed-Time Fast Integral Terminal Sliding Mode Speed Control Strategy with Super-Twisting Observer for SPMSM

Qianghui Xiao, Zheng Xiong*, Li Yang, Dengliang Xia, Xing Yuan, and Sheng Wang

Hunan University of Technology, Zhuzhou 412007, China

ABSTRACT: To improve the dynamic performance and disturbance rejection of a Surface Permanent Magnet Synchronous Motor (SPMSM) speed control system, a speed regulation method based on a continuous adaptive fast terminal sliding mode is proposed in this study. First, a novel adaptive variable-gain reaching law (NVGRL) is introduced. By combining variable gains of system states with fuzzy adaptive inference rules, the boundary layer width was adjusted in real time to reduce the convergence time to the equilibrium point and suppress chattering. Second, a novel fast integral terminal sliding mode surface (NFITSMS) is designed to improve the global convergence rate. To maintain an ideal speed even under external disturbances and torque surges, a novel finite-time-based super-twisting sliding mode disturbance observer (NSTDO) is designed. The control strategy proposed in this study employs Lyapunov stability theory to provide a closed-loop stability analysis within a fixed time. Finally, the experimental results confirm that the proposed method enhances the speed response, tracking accuracy, and disturbance rejection capability of the SPMSM control system.

1. INTRODUCTION

Permanent magnet synchronous motors (PMSMs) are high-performance, high-efficiency motors widely used in high-speed rail, aerospace, electric vehicles, robotics, and industrial servo systems [1, 2]. Compared with integrated permanent magnet synchronous motors (IPMSMs), surface-mounted permanent magnet synchronous motors (SPMSMs) offer significant advantages, including a simple structure, compact size, light weight, low manufacturing costs, and fewer magnetic flux harmonic components [6]. In addition, SPMSMs feature simple control methods and low torque ripple, and are widely used due to their high efficiency, high power density, and high torque-to-inertia ratio [6]. However, as nonlinear, multivariable systems with strong coupling effects [5], SPMSMs are susceptible to a range of uncertainties during operation [6]. This results in traditional vector-based proportional-integral (PI) controllers performing poorly when they face system nonlinearities, time-varying parametric uncertainties, and outside disturbance factors [7]. To overcome these limitations, advanced control strategies, such as model predictive control [8], adaptive control [9], robust control [10], and intelligent control [11], have been introduced in the field of PMSM control.

Among them, sliding mode control (SMC) is extensively adopted for nonlinear systems because of its strong robustness against matched uncertainties and design independence from exact models [12, 13]. Nevertheless, traditional SMC fails to converge within a finite time, and the high-frequency oscillations it exhibits can easily lead to mechanical wear and control signal noise. This phenomenon stems from the discontinuous characteristic of the control law as well as the frequent switching behavior around the sliding mode surface [14]. At present, extensive studies focus on sliding mode control methods, which are classified into three categories: adaptive design, nonlinear and high-order sliding surface modification, and disturbance observer compensation. The first category addresses the issues of slow convergence and excessive oscillation by adaptively adjusting the gain of the reaching law or sliding surface. In [15], researchers devised a modified composite adaptive sliding reaching law by adopting sliding mode control theory, which is capable of effectively improving the dynamic speed-tracking performance of PMSM drive systems. In [16], a terminal reaching law incorporating adaptive power-order terms is introduced into the reaching law to accelerate PMSM response and alleviate oscillation. In [17], an adaptive saturation function is designed using fuzzy logic to reduce steady-state error. The second category determines the convergence characteristics of the sliding model by designing the sliding surface. Among them, non-singular fast-terminating sliding modes [18–20] achieve the finite-time convergence of the state via nonlinear terms. The integral terminal sliding surface [21] can effectively eliminate steady-state errors. In [22], an improved fast-terminating sliding surface is adopted, while an optimized predefined-time sliding-mode predictive control method is proposed to obtain excellent disturbance suppression and tracking accuracy. The third research category adopts disturbance observers to realize real-time estimation and feedforward compensation of system lumped disturbances, which alleviates the control pressure of the sliding mode control algorithm. This allows for the use of smaller switching gains to suppress oscillations [23]. Examples include a non-singular fast-terminating sliding-mode disturbance observer [24], a high-gain disturbance observer [25], and a hyper-helix disturbance observer [26], among others.

* Corresponding author: Zheng Xiong (1940168033@qq.com).

To address the gaps identified in the available research, this study proposes a novel fast terminal integral sliding mode control (NFITSMC) strategy. This approach enhances SPVWM speed control, reduces steady-state error, and significantly improves the disturbance-rejection performance. First, the NVGRL is adopted to balance the convergence rate and chattering suppression. It employs a variable boundary-layer saturation function that adjusts the boundary-layer width in real time by designing fuzzy and adaptive inference rules. Meanwhile, adaptive gains related to the system states and variable exponential terms are introduced. This approach enables rapid global tracking within a fixed time window while effectively reducing chattering. Second, an NFITSMS is proposed to ensure convergence within a finite time while improving the convergence rate both far from and near the equilibrium point, thereby achieving faster global speed tracking. Third, an NSTDO was developed to enhance robustness against internal and external disturbances and to improve dynamic and steady-state performance.

The remainder of this paper is organized as follows. Section 2 develops the mathematical model of the SPMSM. Section 3 elaborates the design procedure and stability analysis of the developed controller integrating NVGRL and NFITSMS. Section 4 details the design and stability verification of the NSTDO. Section 5 presents experimental verification to confirm the effectiveness of the proposed approach. Finally, the entire research work is concluded and summarized.

2. MATHEMATICAL MODEL OF SPMSMS

For the convenience of theoretical derivation and modeling analysis, several reasonable simplifying assumptions were adopted when building the mathematical model of the PMSM: (1) the saturation effect of the motor stator iron core was ignored; the magnetic circuit was regarded as linear; and all inductance parameters were kept constant; (2) iron-core eddy-current and hysteresis losses were ignored in this modeling process; (3) the rotor permanent magnet material was assumed to have negligible electrical conductivity; (4) the rotor structure was designed without additional damping windings; and (5) the stator three-phase current of the motor is considered to be balanced and sinusoidal. Based on the above assumptions, the mathematical model of the PMSM under the d-q coordinate system is established as follows:

$$J\frac{dw_m}{dt} = T_e - T_L - Bw_m \tag{1}$$

$$T_e = \frac{3}{2}P_n\varphi_f i_q \tag{2}$$

$$\begin{cases} u_d = R_s i_d + L_d\dfrac{di_d}{dt} - L_q w_e i_q \\ u_q = R_s i_q + L_q\dfrac{di_q}{dt} + L_d w_e i_d + w_e\varphi_f \end{cases} \tag{3}$$

where J is the moment of inertia; w_m is the mechanical angular velocity; t is the time; T_e is the electromagnetic torque; T_L is the load torque; B is the coefficient of viscous friction; P_n is the number of pole pairs; φ_f is the magnetic flux of the permanent magnet; i_d, i_q, u_d, u_q are motor currents and voltages on the d and q axes, respectively; R_s is the stator resistance; L_d and L_q are the inductances of the d and q axes, respectively, and for the SPMSM, $L_d = L_q$.

3. NOVEL SLIDING MODE SPEED CONTROLLER

3.1. NVGRL Design

In sliding mode control, the reaching law is a core component of the controller design. The design of the reaching law directly affects the convergence rate, disturbance-rejection capability, and ability to suppress system oscillations.

Define state variables:

$$\begin{cases} X_1 = w_m^* - w_m \\ X_2 = \dot{X}_1 = \dot{w}_m^* - \dfrac{T_e - T_L - Bw_m}{J} \end{cases} \tag{4}$$

To balance convergence rate and oscillation suppression, the NVGRL is proposed by combining the system state error, variable-exponent term, and adaptive gain. The reaching law is as follows:

$$\dot{s} = -b\left(e^{k_1|x_1|} - 1\right)\cdot H(s) - k_2|s|^{r\cdot\mathrm{sign}(|s|-1)}\cdot s \tag{5}$$

where $b > 0$, $k_1 > 0$, $k_2 > 0$, $0 < r < 1$.

The reaching law consists of two parts:

The first item: the state variables are introduced into the coefficients of the constant-speed convergence term, thereby achieving a variable-gain effect. When the state variable $|X_1|$ is large (i.e., the SMC trajectory is far from the sliding surface), $K_1X_1 > K_1$, thus accelerating the convergence. As the moving point approaches the equilibrium point on the sliding surface, the convergence rate decreases as X_1 decreases. The constant-speed term gradually decreased and eventually converged to 0, thereby effectively suppressing oscillations. In addition, this study replaces the traditional saturation function with the novel saturation function $H(s)$ which is defined as follows:

$$H(s) = \frac{2}{\pi}\arctan\left(\frac{k\pi}{2}s\right) \tag{6}$$

where $k > 0$.

Traditional saturation functions switch between linear segments inside and outside the boundary layer, resulting in abrupt changes in their derivatives at the boundary points. This discontinuity is the root cause of significant oscillations. In contrast, the newly designed saturation function is based on a smooth inverse-tangent characteristic, featuring a continuous, rapidly decaying derivative across the entire domain. This generates an exceptionally smooth control signal, filters out chattering at its source, and provides the motor with smoother, more precise speed control. In addition, the parameter k offers greater flexibility than the traditional boundary layer thickness: increasing

k results in a steeper slope of the function near the origin, accelerating the convergence of the system state to the sliding surface; decreasing k further enhances the smoothing effect to suppress oscillations under extreme operating conditions. A comparison of $H(s)$ functions with different values of k is shown in Fig. 1.

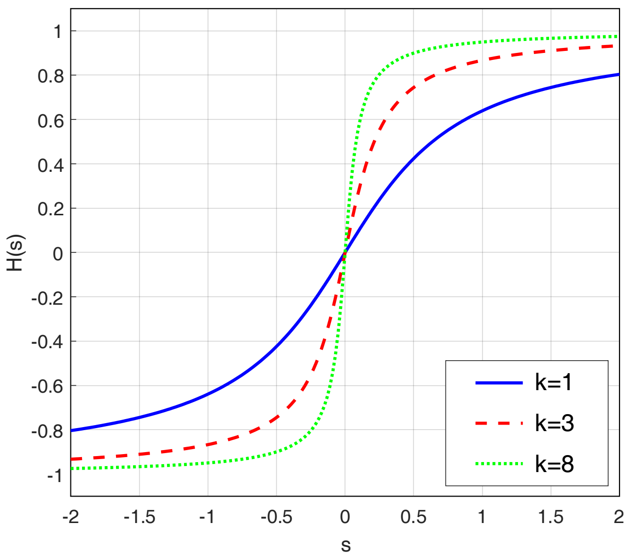

FIGURE 1. Comparison of $H(s)$ functions with different k values.

To further reduce oscillations and improve the system dynamic performance, a fuzzy control system was designed to adaptively adjust the parameter k. This allows for the real-time adjustment of the novel saturation function $H(s)$ to balance oscillation suppression with response speed. The sliding surface is defined as the input variable of the fuzzy controller with a domain of $[-105, 105]$. Parameter k is defined as the output variable with a domain of $[1, 8]$. The designed fuzzy rules are listed in Table 1.

TABLE 1. Fuzzy rule table.

s	NB	NM	NL	NS	Z	PL	PS	PM	PB
k	PB	PM	PS	PL	Z	PL	PS	PM	PB

The Mamdani algorithm was adopted to fuzzify the input variables, and the centroid algorithm was used for defuzzification. Through the designed rules, parameter k can be adjusted in real time to obtain the optimal saturation function, balancing vibration suppression and response speed.

The second item: This term adds coefficients of the powers of the absolute value of s to the exponential series. When $s > 1$, $\text{sign}(s) = 1$ and $\text{sign}(|s| - 1) = 1$. In this case, the convergence rate is $k_2|s|^r * s$. When the system operating state is far away from the sliding surface, it achieves a quicker convergence rate than the conventional exponential convergence term. When the system position approaches the sliding surface (i.e., $1 > s > 0$), $\text{sign}(s) = 1$, but $\text{sign}(|s| - 1) = -1$. At this point, $k_2|s|^{-r*}s > k_2 s > k_2|s|^{r*}s$. This method effectively solves the problem of slow dynamic convergence and uncertain convergence time of conventional exponential reaching laws in the vicinity of the sliding surface. Meanwhile, it achieves a higher convergence rate than the terminal sliding mode reaching laws. Accordingly, compared with conventional exponential reaching laws and terminal sliding mode reaching laws, the proposed scheme has two distinct advantages: a higher convergence rate and a suppressed chattering level.

Compared with the enhanced composite adaptive sliding mode reaching law in [15] and the improved terminal reaching law with adaptive power terms in [16], the NVGRL proposed in this paper exhibits superior overall performance: the former only adaptively adjusts the gain of the constant-speed term and retains the traditional piecewise saturation function, where abrupt changes in the boundary layer derivative can easily induce control chattering; the latter, although it optimizes the convergence dynamics, still relies on the initial state for the upper bound of the convergence time and lacks sufficient smoothness near the slip surface. Through the coordinated design of state-dependent variable gain, piecewise variable exponential terms, and a fuzzy adaptive inverse tangent saturation function, the NVGRL achieves both faster global convergence and superior vibration suppression, with a global upper bound on convergence time that is independent of the initial state.

3.2. NFITSMS Design

In SMC, the sliding surface determines the system trajectory. By combining the integrative and terminal sliding modes, the need for velocity derivative information is eliminated. Furthermore, the introduction of a nonlinear component into the sliding mode control strategy can accelerate convergence of the velocity error, enabling the system to achieve finite-time convergence. The sliding surface is defined as follows:

$$s = X_1 + \int_0^t \lambda_1 \text{sign}^{1+\varsigma}(X_1) + \lambda_2 \text{sign}^{1-\varsigma}(X_1) + \lambda_3 |X_1| e^{-\mu|X_1|} \text{sign}(X_1)\, dt \tag{7}$$

where λ_1, λ_2, λ_3 are all greater than zero, $0 < \zeta < 1$, $\mu > 0$.

On this sliding surface, the tracking error converges to the origin within a fixed time, regardless of the initial state. When the system state is distant from the equilibrium point, $\lambda_1 \text{sign}^{1+\zeta}(X_1)$ plays a dominant role in guaranteeing fast convergence. As the system state moves close to equilibrium, the system converges quickly under the action of $\lambda_2 \text{sign}^{1-\zeta}(X_1)$. Meanwhile, when the system state is far from equilibrium, the effect of $\lambda_3 |X_1| e^{-\mu|X_1|} \text{sign}(X_1)$ is negligible, preventing the integrator from becoming deeply saturated. Furthermore, this term can regulate the convergence rate as the system state approaches equilibrium and ensures finite-time convergence of the system, ultimately achieving rapid global convergence of the tracking error. Compared with conventional fixed-time terminal sliding surfaces relying only on bilateral power terms [24], the proposed NFITSMS introduces an exponential-attenuation nonlinear term to overcome their inherent drawbacks: integrator saturation under large initial errors and slow convergence near the equilibrium point.

3.3. NFITSMC Design

Taking the derivative of Eq. (7) and setting it equal to Eq. (5) yields the following control law:

$$\begin{aligned} i_q^* = & \frac{2J}{3P_n\varphi_f}\Big[\frac{B}{J}w_m+\frac{T_L}{J}+\lambda_1\mathrm{sign}^{1+\varsigma}(X_1) \\ & +\lambda_2\mathrm{sign}^{1-\varsigma}(X_1)+\lambda_3|X_1|e^{-\mu|X_1|}\mathrm{sign}(X_1) \\ & +b\left(e^{k_1|x_1|}-1\right)\cdot H(s)+k_2|s|^{r\cdot\mathrm{sign}(|s|-1)}\cdot s\Big] \end{aligned} \tag{8}$$

In the proposed speed controller, increasing the reference gains k_1 and k_2 of the reaching law can accelerate the convergence speed of sliding mode states and enhance the robustness against load disturbances and parameter mismatch, but tends to aggravate steady-state current chattering. The power exponent r regulates the convergence rate difference between the sliding surface regions far from and near the equilibrium point, while the boundary layer parameter k determines the smoothness of the arctangent saturation function; both of them need to be traded off between rapidity and smoothness, and the dynamic optimization of the boundary layer parameter is realized via fuzzy adaptive rules in this paper. For the sliding surface, the nonlinear term coefficient λ_1 dominates the error convergence speed, and its increase speeds up the dynamic response but easily causes speed overshoot. The linear term coefficient λ_2 determines the system damping strength. Enlarging it can improve the anti-disturbance robustness and reduce speed drop, yet will prolong the system settling time. The exponential attenuation term coefficient λ_3 and attenuation factor μ are applied to optimize convergence near the equilibrium point, and their reasonable tuning can improve steady-state tracking accuracy and avoid low-frequency oscillation. The power exponent ζ tunes the nonlinear convergence: a smaller ζ accelerates convergence but risks overshoot, while a larger ζ smooths the transient at the cost of slower response. Combining this with dynamic Eq. (8), the corresponding control law block diagram is shown in Fig. 2.

3.4. Stability Analysis

Lemma 1 [27]: For the system $\dot{x}=f(x)$, $f(0)=0$, and $x\in R^n$. Assume that there exists a continuous, positivedefinite and radially unbounded Lyapunov function $V(x)$ satisfying the following conditions:

$$\dot{V}(x)\le -a\cdot[V(x)]^p-b[V(x)]^q,\quad \forall x\in U_0 \tag{9}$$

where $a>0$, $b>0$, $p>1$, $0<q<1$.

Thus, the system is not only finitely time-stable but also fixed-time-stable. It means that for any initial state $x_0\in U_0$, the system trajectory $x(t)$ reaches the origin at some finite time $T(x_0)$ and remains at the origin thereafter. The convergence time $T(x_0)$ with a global upper bound $T_{\max}$ that is independent of the initial state x_0 is

$$T(x_0)\le T_{\max}=\frac{1}{a(p-1)}+\frac{1}{b(1-q)},\quad \forall x_0\in R^n \tag{10}$$

Lemma 2: Consider the system up to $\dot{x}=f(x)$, $f(0)=0$, and $x\in R^n$. Suppose that there exists a continuous, positive-definite, radially unbounded function $V(x)$ such that:

$$\dot{V}(x)\le -a_1\cdot[V(x)]^{p_1}-b_1[V(x)]^{q_1},\quad \forall x\in U_0 \tag{11}$$

where $a_1>0$, $b_1>0$, $p_1=1+1/\mu_1$, $q_1=1-1/\mu_1$, $\mu_1>1$.

Then, the origin of the system is a stable equilibrium point at a fixed time, and the convergence time $T(x_0)$ satisfies

$$T(x_0)\le T_{\max}=\frac{\mu_1\pi}{2\sqrt{a_1b_1}} \tag{12}$$

Proof: Let $z=V^{1/\mu_1}$, $z(0)=V(0)^{1/\mu_1}$, then integrate and transform Eq. (11) to yield:

$$\begin{aligned} T &= \int_0^{V(0)}\frac{dV}{a_1\cdot[V(x)]^{p_1}+b_1[V(x)]^{q_1}} \\ &= \int_0^{z(0)}\frac{\mu_1 z^{\mu_1-1}dz}{z^{\mu-1}(a_1z^2+b_1)} \\ &= \int_0^{z(0)}\frac{\mu_1 dz}{a_1z^2+b_1} \\ &= \frac{\mu_1}{\sqrt{a_1b_1}}\arctan\left(\sqrt{\frac{a_1}{b_1}}z(0)\right) \\ &\le \frac{\mu_1\pi}{2\sqrt{a_1b_1}} \end{aligned} \tag{13}$$

Lemma 3: Let $V(x)$ be a continuous positive-definite function. There exist constants $\mu_2>0$, $c>0$, $d>0$, $p_2>1$, and $0<q_2<1$ such that that equation (14) holds.

$$\dot{V}(x)\le\begin{cases}-cV(x)^{p_2} & V(x)\ge\mu_2,\\ -dV(x)^{q_2} & 0<V(x)\le\mu_2,\end{cases} \tag{14}$$

Consequently, the system achieves finite-time stability at the equilibrium point, with the convergence time T satisfying the following constraint:

$$T\le\frac{\mu^{1-p_2}}{c(p_2-1)}+\frac{\mu^{1-q_2}}{d(1-q_2)} \tag{15}$$

Proof:

$$\begin{aligned} T &\le \int_0^{\mu_2}\frac{dV}{dV^{q_2}}+\int_{\mu_2}^{\infty}\frac{dV}{cV^{p_2}} \\ &= \frac{1}{d}\int_0^{\mu_2}V^{-q_2}dV+\frac{1}{c}\int_{u_2}^{\infty}V^{-p_2}dV \\ &= \frac{1}{d}\left(\frac{\mu_2^{1-q_2}}{1-q_2}-\frac{0^{1-q_2}}{1-q_2}\right)+\frac{1}{c}\left(0-\frac{\mu_2^{1-p_2}}{1-p_2}\right) \\ &= \frac{\mu_2^{1-q_2}}{d(1-q_2)}+\frac{\mu_2^{1-p_2}}{c(p_2-1)} \end{aligned} \tag{16}$$

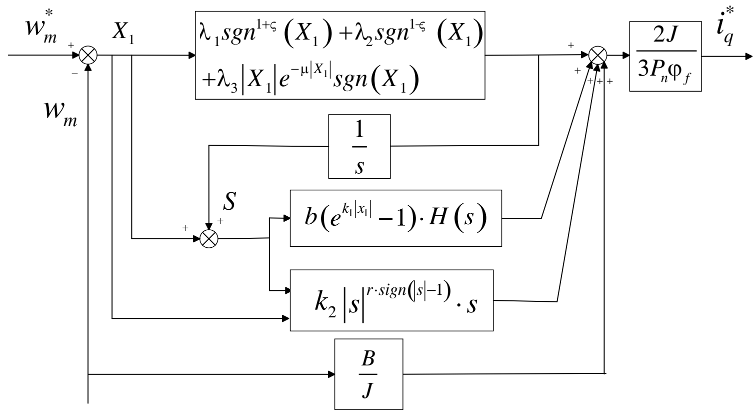

FIGURE 2. Speed control block diagram.

The proof of controller stability can be divided into two stages. The first stage is the approach phase, during which the system state moves toward the sliding surface under the action of the convergence law. The second stage is the sliding phase, during which the system state continues to move along the sliding surface until it converges to the origin.

Approach phase: A Lyapunov function is formulated as follows:

$$V_1 = \frac{1}{2}s^2 \tag{17}$$

Taking the derivative of Eq. (17) yields:

$$\begin{aligned} V_1 &= s\dot{s} \\ &= s\left[-b\left(e^{k|X_1|}-1\right)\cdot H(s) - k_2 |s|^{r\cdot \mathrm{sign}(|s|-1)}\cdot s\right] \\ &= -b\left(e^{k|X_1|}-1\right)\cdot H(s)\cdot s - k_2 |s|^{2+r\cdot \mathrm{sign}(|s|-1)} \end{aligned} \tag{18}$$

Due to the properties of the saturation function, $H(s)*s > 0$. Since $k|\ X_1| > 0$, $e^{k|X_1|} - 1 > 0$. Therefore, the first term $-b(e^{k|X_1|} - 1) * H(s) * s < 0$. Therefore, we obtain Eq. (19)

$$V_1 \le -k_2 |s|^{2+r\cdot \mathrm{sign}(|s|-1)} \tag{19}$$

Substituting $|s| = \sqrt{2V_1}$ into Eq. (19) yields:

$$\dot{V}_1 \le \begin{cases} -2^{\frac{2+r}{2}} k_2 V^{\frac{2+r}{2}}, & V > \frac{1}{2} \\ -2^{\frac{2-r}{2}} k_2 V^{\frac{2-r}{2}}, & V \le \frac{1}{2} \end{cases} \tag{20}$$

Since $b > 0$, $k_1 > 0$, $k_2 > 0$, $0 < r < 1$, we have $c = 2^{(2+r)/2}k_2 > 0$, $d = 2^{(2-r)/2}k_2 > 0$, $\mu_2 = 1/2 > 0$, and $p_2 = (2+r)/2 > 1$, $0 < q_2 = (2-r)/2 < 1$, which atisfies Lemma 3. By Lemma 3, the system converges to the sliding surface within a fixed time T_1 as follows:

$$T_1 \le \frac{2^{-r/2}}{r2^{-r/2}} + \frac{2^{r/2}}{r2^{r/2}} = \frac{2}{r} \tag{21}$$

Sliding segment: As the system state moves along the predefined sliding surface, $s = 0$ holds. Eq. (7) can be expressed as:

$$\begin{aligned} X_2 = &-\lambda_1 \mathrm{sign}^{1+\varsigma}(X_1) + \lambda_2 \mathrm{sign}^{1-\varsigma}(X_1) \\ &+\lambda_3 |X_1| e^{-\mu|X_1|}\mathrm{sign}(X_1) \end{aligned} \tag{22}$$

Construct the following Lyapunov function:

$$V_2 = \frac{1}{2}X_1^2 \tag{23}$$

Taking the derivative of Eq. (23) yields:

$$\begin{aligned} \dot{V}_2 &= X_1 \cdot X_2 \\ &= -X_1[\lambda_1 \mathrm{sign}^{1+\varsigma}(X_1) + \lambda_2 \mathrm{sign}^{1-\varsigma}(X_1) \\ &\quad + \lambda_3 |X_1| e^{-\mu|X_1|}\mathrm{sign}(X_1)] \\ &= -\left[\lambda_1 |X_1|^{2+\varsigma} + \lambda_2 |X_1|^{2-\varsigma} + \lambda_3 |X_1|^2 e^{-\mu|X_1|}\right] \\ &\le -\left[\lambda_1 |X_1|^{2+\varsigma} + \lambda_2 |X_1|^{2-\varsigma}\right] \end{aligned} \tag{24}$$

Substituting $|X_1| = \sqrt{2V}$ into Eq. (24) yields:

$$\dot{V}_2 \le -\lambda_1 2^{1+\frac{\varsigma}{2}} V^{1+\frac{\varsigma}{2}} - \lambda_2 2^{1-\frac{\varsigma}{2}} V^{1-\frac{\varsigma}{2}} \tag{25}$$

where $2^{(1+\zeta)/2} > 0$, $2^{(1-\zeta)/2} > 0$, and the two indices are inversely related and symmetric about 1. Satisfies Lemma 2. From Lemma 2, it follows that the speed error X_1 converges to a small neighborhood within a fixed time T_2, where $\mu_1 = 2/\zeta$, $a_1 = \lambda_1 2^{1+\varsigma/2}$, $b_1 = \lambda_2 2^{1-\varsigma/2}$, and T_2 satisfies:

$$\begin{aligned} T_2 &\le \frac{\mu_1 \pi}{2\sqrt{a_1 b_1}} = \frac{(2/\varsigma)\pi}{2\sqrt{(\lambda_1 2^{1+\varsigma/2})(\lambda_2 2^{1-\varsigma/2})}} \\ &= \frac{\pi}{\beta\sqrt{\lambda_1\lambda_2 2^2}} = \frac{\pi}{2\varsigma\sqrt{\lambda_1\lambda_2}} \end{aligned} \tag{26}$$

In summary, the PMSM dynamic system is time-invariantly stable under the proposed control law. Furthermore, the system state reaches the equilibrium point in a fixed time that does not rely on the initial states. The upper bound on the convergence time T is

$$T = T_1 + T_2 \leq \frac{2}{r} + \frac{\pi}{2\varsigma\sqrt{\lambda_1\lambda_2}} \tag{27}$$

4. NSTDO DESIGN

During actual operation, electric motors are subjected to various factors. When parameter mismatches are considered in the actual operation of SPMSMs, the equations of motion for SPMSMs can be expressed as:

$$\begin{aligned}\dot{w}_m &= \frac{3p_n(\varphi_f+\Delta\varphi_f)}{2(J+\Delta J)}i_q - \frac{1}{(J+\Delta J)}T_L - \frac{(B+\Delta B)}{(J+\Delta J)}w_m \\ &= (\alpha+\Delta\alpha)i_q - (\beta+\Delta\beta)T_L - (\gamma+\Delta\gamma)w_m\end{aligned} \tag{28}$$

where $\Delta\alpha = 3p_n(J\Delta\varphi_f - \Delta J\varphi_f)/2J(J+\Delta J)$, $\Delta\beta = -\Delta J/J(J+\Delta J)$, $\Delta\gamma = J\Delta B - B\Delta J/J(J+\Delta J)$.

The total disturbance of the system is defined as d, which includes external load disturbances and internal parameter variations, and can be expressed as:

$$\frac{d}{J} = (\beta+\Delta\beta)T_L + \Delta\gamma w_m - \Delta\alpha i_q \tag{29}$$

Eq. (28) can be rewritten as:

$$\dot{w}_m = \frac{3P_n\varphi_f}{2J}i_q - \frac{B}{J}w_m - \frac{d}{J} \tag{30}$$

The q-axis current considering the total disturbance can be obtained from Eqs. (5), (7), and (30) as follows:

$$\begin{aligned}i_q^* = \frac{2J}{3P_n\varphi_f}\Big[&\frac{B}{J}w_m + \frac{d}{J} + \lambda_1\mathrm{sign}^{1+\varsigma}(X_1) + \lambda_2\mathrm{sign}^{1-\varsigma}(X_1) \\ &+\lambda_3|X_1|e^{-\mu|X_1|}\mathrm{sign}(X_1) + b\left(e^{k_1|x_1|}-1\right)\cdot H(s) \\ &+k_2|s|^{r\cdot\mathrm{sign}(|s|-1)}\cdot s\Big]\end{aligned} \tag{31}$$

As shown in (30), internal and external disturbances exert a remarkable influence on the controller performance. To enhance the robustness of the controller against such disturbances, the NSTDO was designed to estimate disturbances in real time and provide compensation for the i_q^* component via feedback. By treating the disturbance variable as an extended state variable of the system, Eq. (30) can be rewritten as

$$\begin{cases}\dot{w}_m = \frac{1}{J}T_e - \frac{B}{J}w_m - \frac{1}{J}d \\ \dot{d} = 0\end{cases} \tag{32}$$

Design NSTDO, which has the following structure:

$$\begin{cases}\dot{\hat{w}}_m = \frac{1}{J}T_e - \frac{B}{J}\hat{w}_m - \frac{1}{J}\hat{d} + \alpha\left[s + e_0^{|s|/2}\sqrt{|s|}\mathrm{sign}(s)\right] \\ \dot{\hat{d}} = \beta\Big[|s| + (0.5|s| + \mathrm{sign}(s) + 0.5)e_0^{|s|/2}\sqrt{|s|} \\ \qquad +0.5e_0^{|s|}(|s|+1)\,\mathrm{sign}(s)\Big]\end{cases} \tag{33}$$

where $\hat{w}_m$ and $\hat{d}$ are the estimates of w_m and d, $\alpha > 0$, $\beta > 0$.

Both conventional fixed-gain and adaptive variable-gain super-twisting observers only achieve finite-time convergence [26], where the convergence time of observation errors increases notably with the initial disturbance deviation, failing to guarantee global convergence consistency. By constructing a novel super-twisting iteration law with piecewise power terms, this design rigorously proves that the observation error system can converge to the neighborhood of the equilibrium point within a fixed time, completely independent of initial errors. The upper bound of the convergence time is determined solely by the observer parameters, ensuring stable and predictable convergence speed regardless of the magnitude of initial disturbance deviations. To accelerate the convergence speed of NSTDO and suppress steadystate errors, an integral term of observation error is added to the conventional linear sliding surface. The adopted integral sliding surface is expressed as follows:

$$s_o = e_o + \frac{B}{J}\int e_o dt \tag{34}$$

where $e_o = \hat{w}_m - w_m$.

Differentiating Eq. (34) yields:

$$\begin{cases}\dot{s}_0 = -\alpha\left[s + e^{|s|/2}\sqrt{|s|}\mathrm{sign}(s)\right] + \frac{z}{J} \\ \dot{z} = -\beta\Big[|s| + (0.5|s| + \mathrm{sign}(s) + 0.5)e^{|s|/2}\sqrt{|s|} \\ \qquad +0.5e^{|s|}(|s|+1)\,\mathrm{sign}(s)\Big] - \dot{d}\end{cases} \tag{35}$$

where $z = \hat{d} - d$.

To prove the stability of the system, Eq. (34) is rewritten as:

$$\begin{cases}\dot{s}_0 = -\alpha\xi_1 + \frac{z}{J} \\ \dot{z} = -\beta\xi_2 - \dot{d}\end{cases} \tag{36}$$

where $\xi_1 = \left[s + e^{|s|/2}\sqrt{|s|}\mathrm{sign}(s)\right]$, $\xi_2 = [|s| + 0.5e^{|s|}(|s|+1)\,\mathrm{sign}(s) + (0.5|s| + \mathrm{sign}(s) + 0.5)e^{|s|/2}\sqrt{|s|}]$.

Assume that $\dot{d}$ is bounded, i.e., $\left|\dot{d}\right| \leq \delta$. Define a new state variable $x = [\xi_1, z]$ and design the Lyapunov function as

$$V = x^T M x \tag{37}$$

where M is a positive-definite matrix, given by:

$$M = \begin{bmatrix}\lambda^2 + 4\eta & -\lambda \\ -\lambda & 2\end{bmatrix} \tag{38}$$

Taking the derivative of ξ_1 with respect to s yields:

$$\xi'_1 = 1 + 0.5e^{|s|/2}\left(\frac{|s|+1}{\sqrt{|s|}}\right) \tag{39}$$

Therefore, the first derivative of ξ_1 is:

$$\dot{\xi}_1 = {\xi'}_1 \dot{s} = {\xi'}_1(-\alpha\xi_1 + \frac{z}{J}) \tag{40}$$

Differentiating $x = [\xi_1, z]$ yields:

$$\dot{x} = {\xi'}_1 \begin{bmatrix} -\lambda & 1/J \\ -\eta & 0 \end{bmatrix} x + \begin{bmatrix} 0 \\ -\dot{d} \end{bmatrix} = {\xi'}_1 Q x + R \tag{41}$$

where

$$Q = \begin{bmatrix} -\lambda & 1/J \\ -\eta & 0 \end{bmatrix}, \quad R = \begin{bmatrix} 0 \\ -\dot{d} \end{bmatrix}$$

According to Eqs. (37)–(41), the first derivative of V is obtained as:

$$\begin{aligned} \dot{V} &= \dot{x}^T M x + x^T M \dot{x} \\ &= {\xi'}_1 x^T \left(Q^T M + MQ\right) x + 2R^T M x \\ &= -{\xi'}_1 x^T N x + \dot{d} L x \end{aligned} \tag{42}$$

where

$$N = \begin{bmatrix} 2\lambda^3 + 6\lambda\eta & -(1+\frac{1}{J})\lambda^2 - (\frac{4}{J} - 2)\eta \\ -(1+\frac{1}{J})\lambda^2 - (\frac{4}{J} - 2)\eta & 2\frac{\lambda}{J} \end{bmatrix},$$

$L = [2\lambda \;\; -4]$.

The Lyapunov function $V = x^T Mx$ satisfies:

$$\lambda_{\min}\{M\}\|x\|_2^2 \le x^T M x \le \lambda_{\max}\{M\}\|x\|_2^2 \tag{43}$$

where $\lambda_{\min}\{M\}$ and $\lambda_{\max}\{M\}$ are the minimum and maximum eigenvalues of matrix M, respectively, and $\|x\|_2^2$ is the Euclidean norm of x. Combining Eqs. (42) and (43) yields

$$\dot{V} \le -{\xi'}_1 \lambda_{\min}\{N\}\|x\|_2^2 + \delta\|L\|_2\|x\|_2 \tag{44}$$

Because:

$$\begin{aligned} {\xi'}_1\|x\|_2 &\ge {\xi'}_1\left[|s| + e^{|s|/2}\sqrt{|s|}\right] \\ &= \left[1 + 0.5e^{|s|/2}(\frac{|s|+1}{\sqrt{|s|}})\right]\left[|s| + e^{|s|/2}\sqrt{|s|}\right] \\ &= |s| + 0.5e^{|s|}(|s|+1) + e^{0.5|s|}\sqrt{|s|} \\ &\quad + 0.5e^{|s|}(|s|+1) \\ &\ge 1 \end{aligned}, \tag{45}$$

from Eqs. (41) and (42), we obtain:

$$\dot{V} \le -\left(\lambda_{\min}\{N\} - \delta\|L\|_2\right)\|x\|_2 \le -\gamma V^{0.5} \tag{46}$$

where γ is defined as:

$$\gamma = \frac{\lambda_{\min}\{N\} - \delta\|L\|_2}{\lambda_{\max}^{0.5}\{M\}} \tag{47}$$

When $\gamma > 0$, i.e., Eq. (48) holds, Lemma 1 is satisfied.

$$\delta < \frac{\lambda_{\min}\{N\}}{\|L\|_2} \tag{48}$$

The above proof shows that the designed NSTDO converges and achieves stability within a specified time. In summary, the gain parameters α and β of the NSTDO are designed primarily based on fixed-time stability criteria and must satisfy the positive-definite constraints of the quadratic matrix Q: $\beta > \delta$ and $\alpha^2 > 2\beta$. α primarily determines the observation response bandwidth, while β governs the steady-state estimation accuracy; the values of these two parameters must strike a balance between convergence rate and oscillation suppression. Based on the motor parameters in this paper, the recommended engineering tuning range is $\alpha \in [600, 2000]$ and $\beta \in [8000, 25000]$. Under light-load steady-state conditions, smaller parameters may be selected to reduce current ripple; under heavy-load disturbance conditions, parameters may be appropriately increased within stability constraints to enhance disturbance-rejection performance. A block diagram of the NSTDO is illustrated in Fig. 3. To realize fast current control of the SPMSM, deadbeat predictive current control is adopted in this paper. The block diagram of the SPMSM control structure, which adopts a speed loop combining the NFITSMC and NSTDO as well as a two-step predictive deadbeat current loop, is shown in Fig. 4.

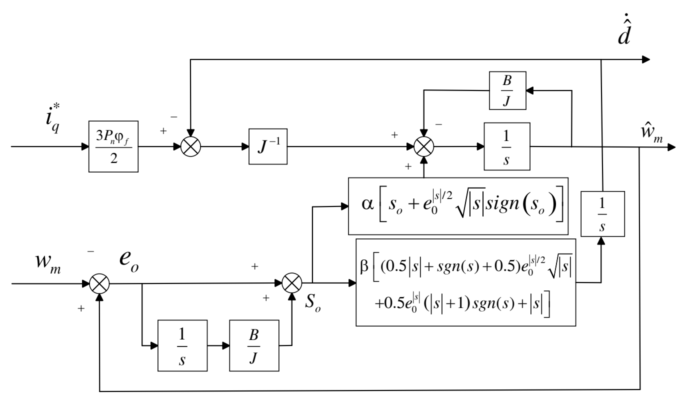

FIGURE 3. Block diagram of the NSTDO.

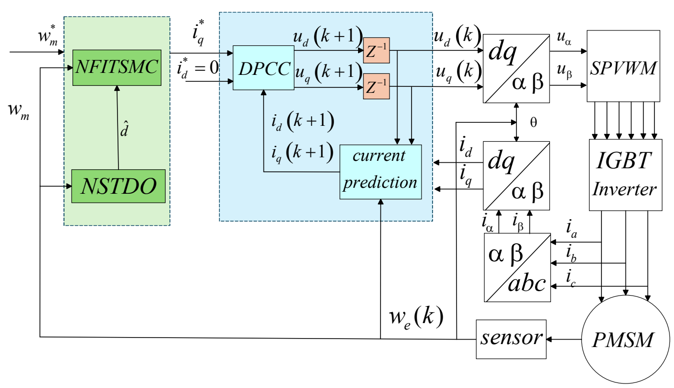

FIGURE 4. Block diagram of the SPMSM system control structure.

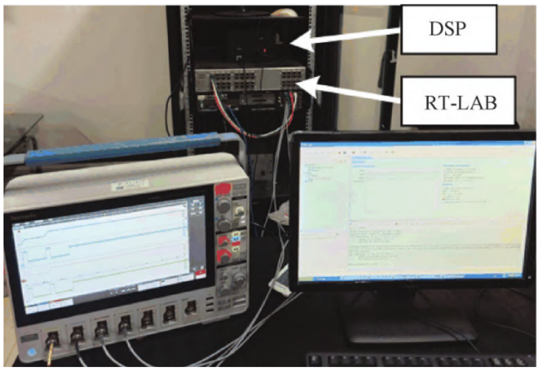

FIGURE 5. RT-LAB experimental platform.

5. EXPERIMENTAL RESULTS AND ANALYSIS

To demonstrate the effectiveness of the proposed control strategy, a series of experiments was conducted. Comparative studies with existing control schemes were conducted to evaluate the performance of the proposed method. The experimental validation was conducted on an RT-LAB platform. The experimental system mainly consisted of a digital signal processing (DSP) control unit, multi-motor system simulation model, OP5600 simulator, and monitoring interface of the host computer. The experimental platform is illustrated in Fig. 5. The SPMSM parameters are listed in Table 2, and the controller parameters of the related methods are presented in Table 3.

TABLE 2. The parameters of SPMSMs.

Symbol	Name	Value
Udc	Direct current voltage	311V
R_S	Stator resistance	0.08 Ω
L	Stator inductance	2 mH
φ_f	Rotor flux linkage	0.062 wb
B	Viscous friction coefficient	0.01 Nm·s/rad
J	Rotational inertia	0.01kg·m^2
P_n	Number of poles	4

TABLE 3. Controller parameters.

Name	Value
ESMRL	$c_1 = 20$, $c_2 = 400$
NVGRL	$b = 900$, $k_1 = 1.5$, $k_2 = 150$, $r = 0.5$
ADRC	$D = 13$, $D_1 = D_3 = 700$, $D_2 = M_2 = 490000$, $M_1 = 1400$, $B = 56.6176$
FITSMS	$p = 40$, $q = 15$, $\lambda = 0.1$
NFITSMS	$\lambda_1 = 5$, $\lambda_2 = 10$, $\lambda_3 = 1350$, $\zeta = 0.4$, $\mu = 4.5$
STDO	$w_1 = 700$, $w_2 = 3500$
NSTDO	$\alpha = 1400$, $\beta = 16000$

To evaluate the performance of the proposed NFITSMS + NVGRL + NSTDO scheme, comparative analyses were conducted using six strategies: FITSMS + ESMRL, ADRC, NFITSMS + ESMRL, NFITSMS + NVGRL, NFITSMS + NVGRL + STDO, NFITSMS + NVGRL + NSTDO. The experiments were designed to measure the speed and q-axis current of the SPMSM under various operating conditions, including the starting process, sudden load variation, and parameter mismatch.

1) load start-up and steady-state performance: shown in Fig. 6, the settling times for the four methods to reach steady state are 0.081 s, 0.08 s, 0.072 s, and 0.067 s, respectively. It can be observed that the proposed NFITSMS combined with NVGRL exhibits a significantly faster response than the other methods. Furthermore, to further evaluate the performance of the proposed strategy, the root mean square error (RMSE) within $0.3 < t < 1$ was calculated, which is defined as

$$RMSE = \sqrt{\frac{1}{N}\sum_{i=1}^{N}\left[w_{ref} - w_e(i)\right]^2} \tag{49}$$

This was used to evaluate the speed response during the steady-state process. The detailed comparison results of the four control methods are listed in Table 4.

2) Speed and current responses under sudden load change and parameter mutation: PMSM parameters are susceptible to sudden variations under actual operating conditions, and there may be deviations between the reference parameters and the actual values. In this experiment, the total operation time is 1.5 s, and the reference speed is set to 1000 rpm. A sudden load of 10 N·m is applied at 0.5 s. At 0.8 s, the permanent magnet flux of the motor suddenly decreases to 0.052 Wb. Meanwhile, the damping coefficient abruptly increases to 0.02 at 1 s. The dynamic responses of rotational speed and $q$axis current are recorded. As illustrated in Fig. 7, in terms of rotational speed, the control strategy integrated with NSTDO can return to the steady state more rapidly under sudden load disturbance and parameter variations. Meanwhile, its speed drop is obviously smaller than that of other control methods. From the perspective of the q-axis current, after the nonlinear variables are observed by the designed NSTDO in this paper, the fluctuation of the current waveform is greatly reduced. As illustrated in Fig. 8, the total harmonic distortion (THD) values of the four control schemes at 1.2 s are 3.75%, 3.25%, 3.18%, and 2.92%, respectively. The proposed control algorithm reduces the harmonic content by 0.83%. Consequently, the combined strategy of NFITSMS + NVGRL + NSTDO can effectively suppress current harmonics. Furthermore, the root mean square error (RMSE) over the time interval $1.1 < t < 1.5$ is computed for each control method to quantify their dynamic performance. The detailed experimental data of the four control strategies are listed in Tables 5–8.

3) Speed and current response to sudden parameter changes under extreme conditions of low speed and heavy load: In this experiment, the total operation time is 1.5 s, and the reference speed is set to 1000 rpm. A sudden load of 12 N·m is applied at 0.5 s. At 0.8 s, the permanent magnet flux of the motor suddenly decreases to 0.052 Wb. Meanwhile, the damping

TABLE 4. Performance indexes of the no-load experiment.

Symbol	Setting time (s)	Speed RMSE	Speed overshoot (rpm)
FITSMS + ESMRL	0.081	0.01731	5
ADRC	0.08	0.01699	4.6
NFITSMS + ESMRL	0.072	0.01193	0.9
NFITSMS + NVGRL	0.067	0.01009	0.75

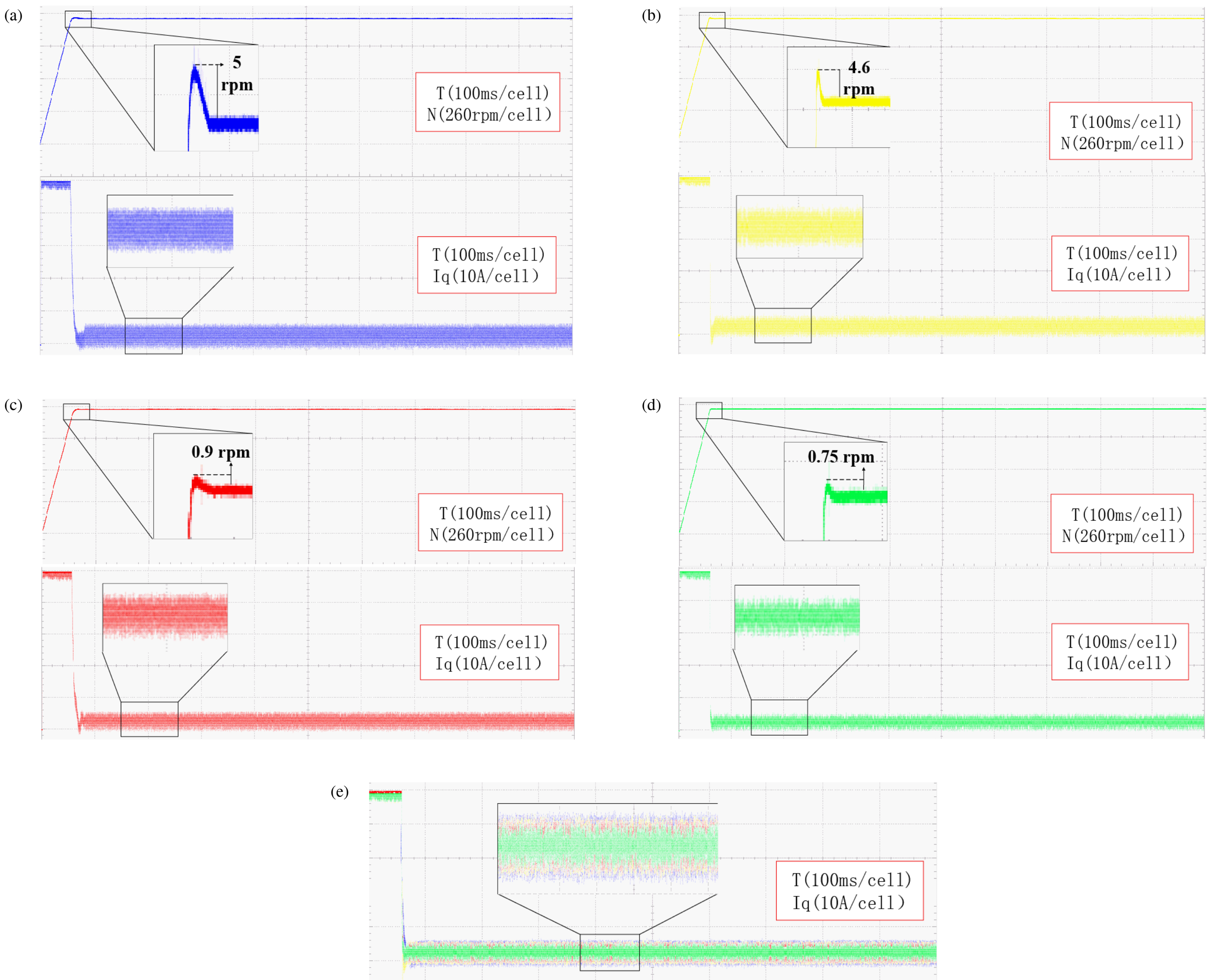

FIGURE 6. Results of the no-load start-up experiment. (a) FITSMS + ESMRL, (b) ADRC, (c) NFITSMS + ESMRL, (d) NFITSMS + NVGRL, and (e) comparison of q-axis current.

coefficient abruptly increases to 0.02 at 1 s. As illustrated in Fig. 9, under extremely low-speed and heavy-load operating conditions, the speed controller proposed in this paper combined with the NSTDO achieves faster dynamic response and smaller current waveform fluctuations than FITSMC, ADRC, and NFITSMC+STDO. As illustrated in Fig. 10, the THD values of the four control schemes at 1.2 s are 3.36%, 3.17%, 3.13%, and 3.08%, respectively. The proposed control algorithm reduces the harmonic content by 0.28%. The RMSE values in the time interval $1.1 < t < 1.5$ are calculated to evaluate the dynamic response performance of the four methods. Detailed experimental data of the four control methods are listed in Tables 9–12.

4) Speed and current response under rotational inertia mismatch in extreme low-speed and heavy-load conditions: Ac-

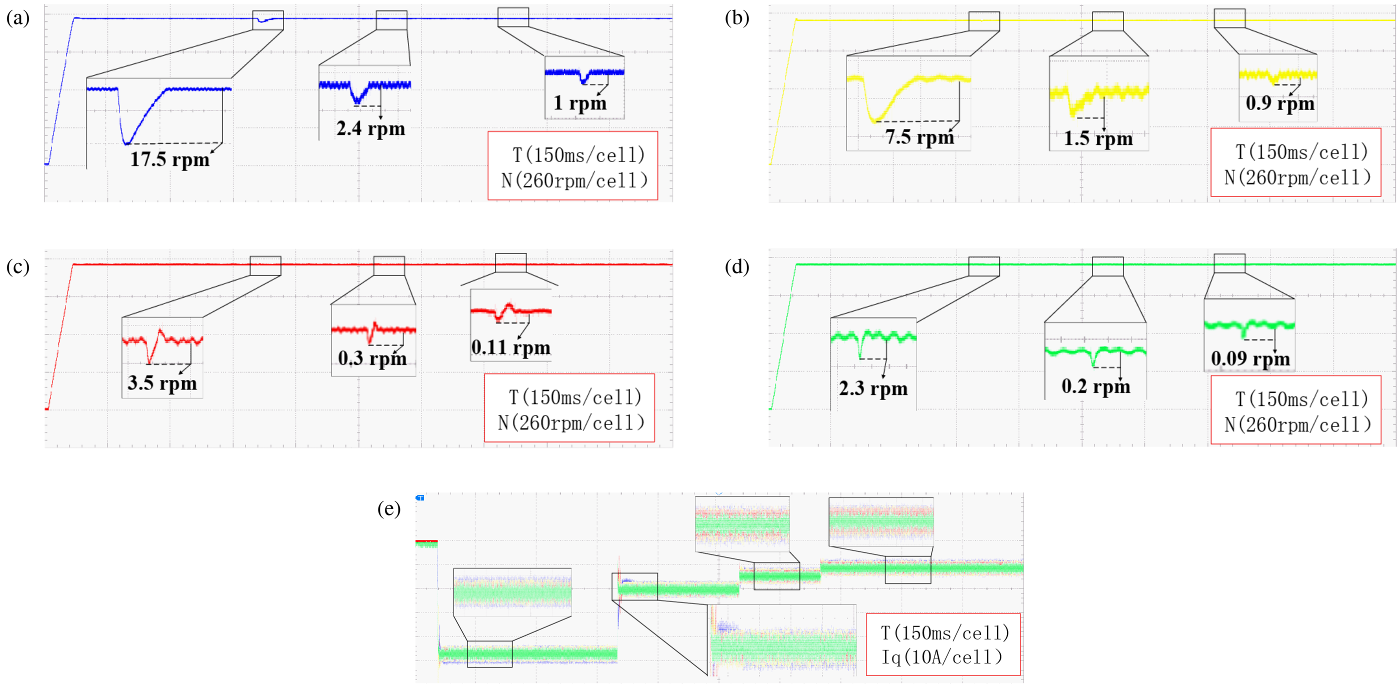

FIGURE 7. Experimental results under sudden load and parameter mutation. (a) FITSMS + ESMRL, (b) ADRC, (c) NFITSMC + STDO, (d) NFITSMC + NSTDO, and (e) Comparison of q-axis current.

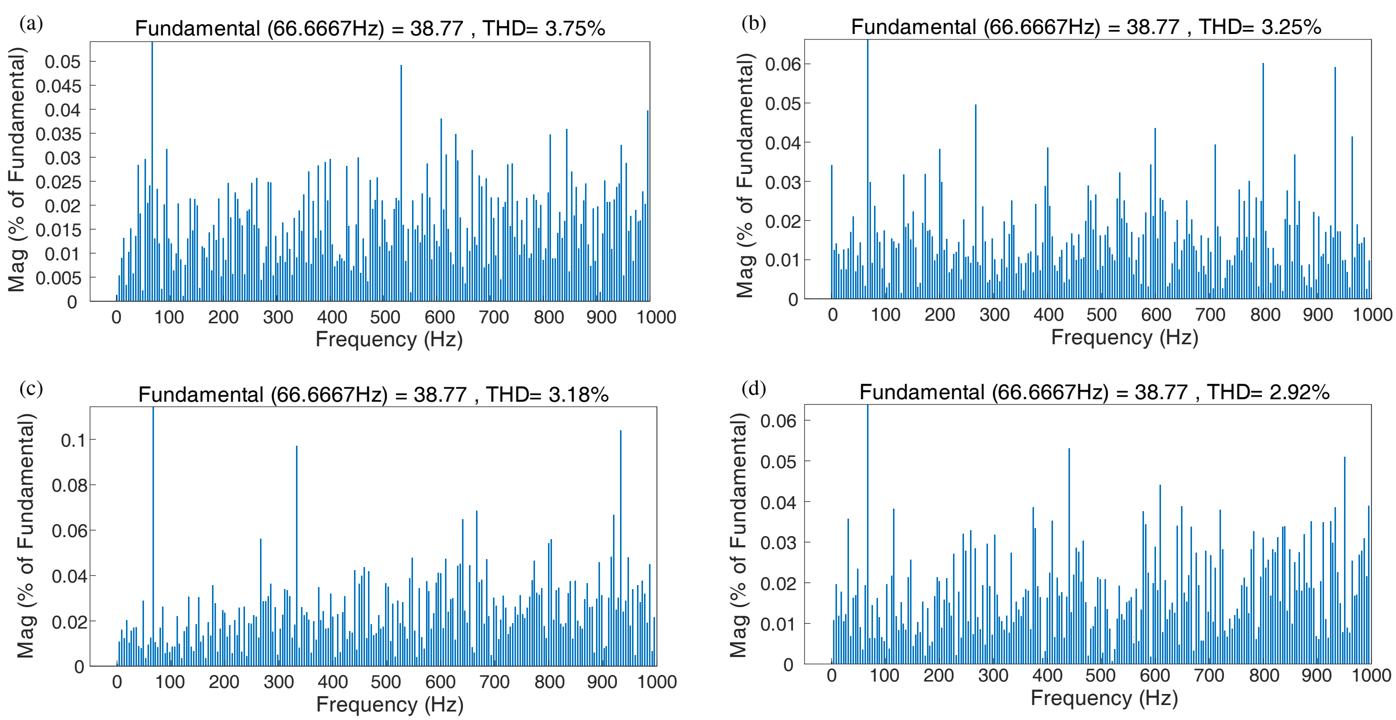

FIGURE 8. THD analysis waveforms at 1.2 s. (a) FITSMS + ESMRL, (b) ADRC (c) NFITSMS + NVGRL + STDO, and (d) NFITSMS + NVGRL + NSTDO.

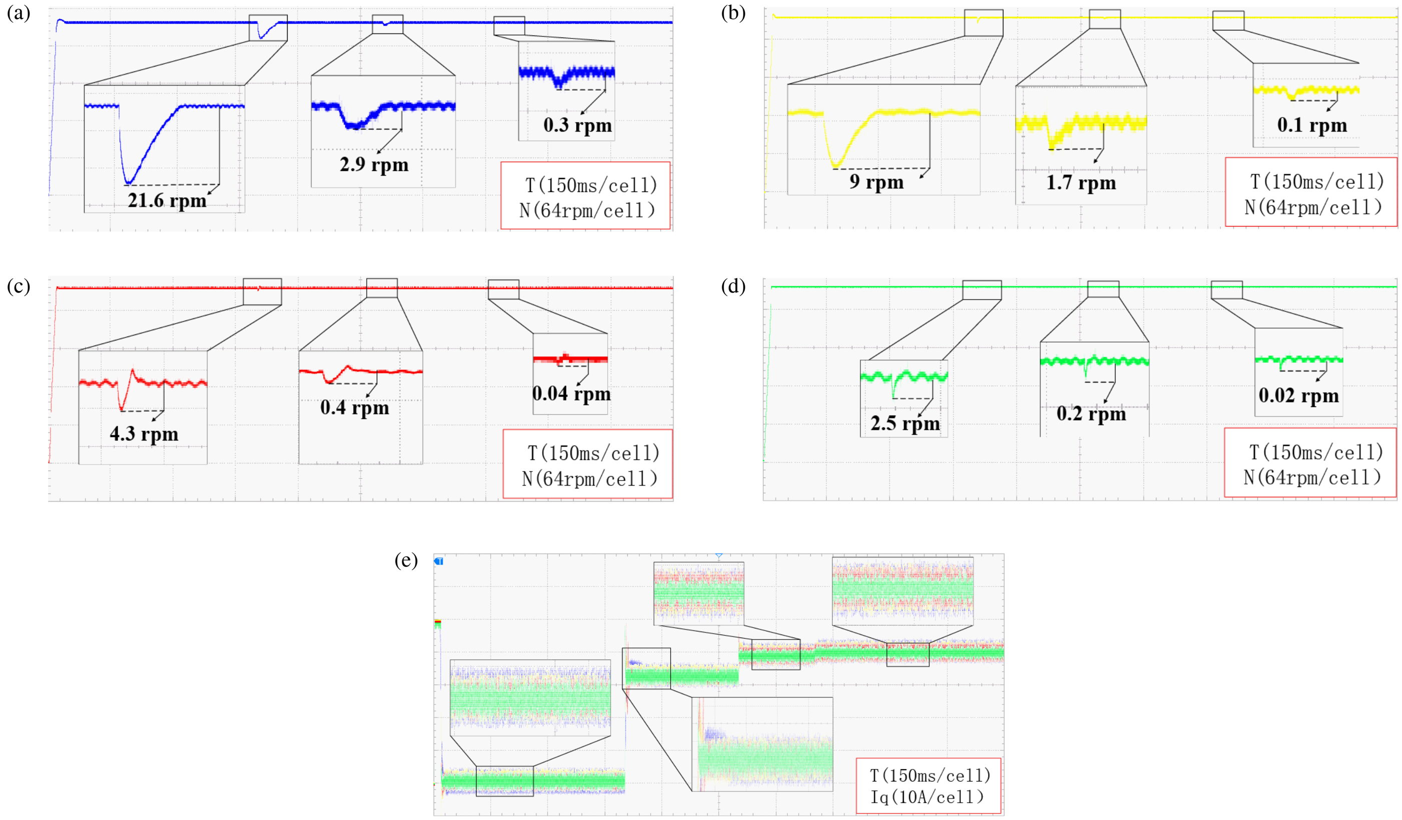

FIGURE 9. Experimental results under low speed and heavy load. (a) FITSMS + ESMRL, (b) ADRC, (c) NFITSMC + STDO, (d) NFITSMC + NSTDO, and (e) comparison of q-axis current.

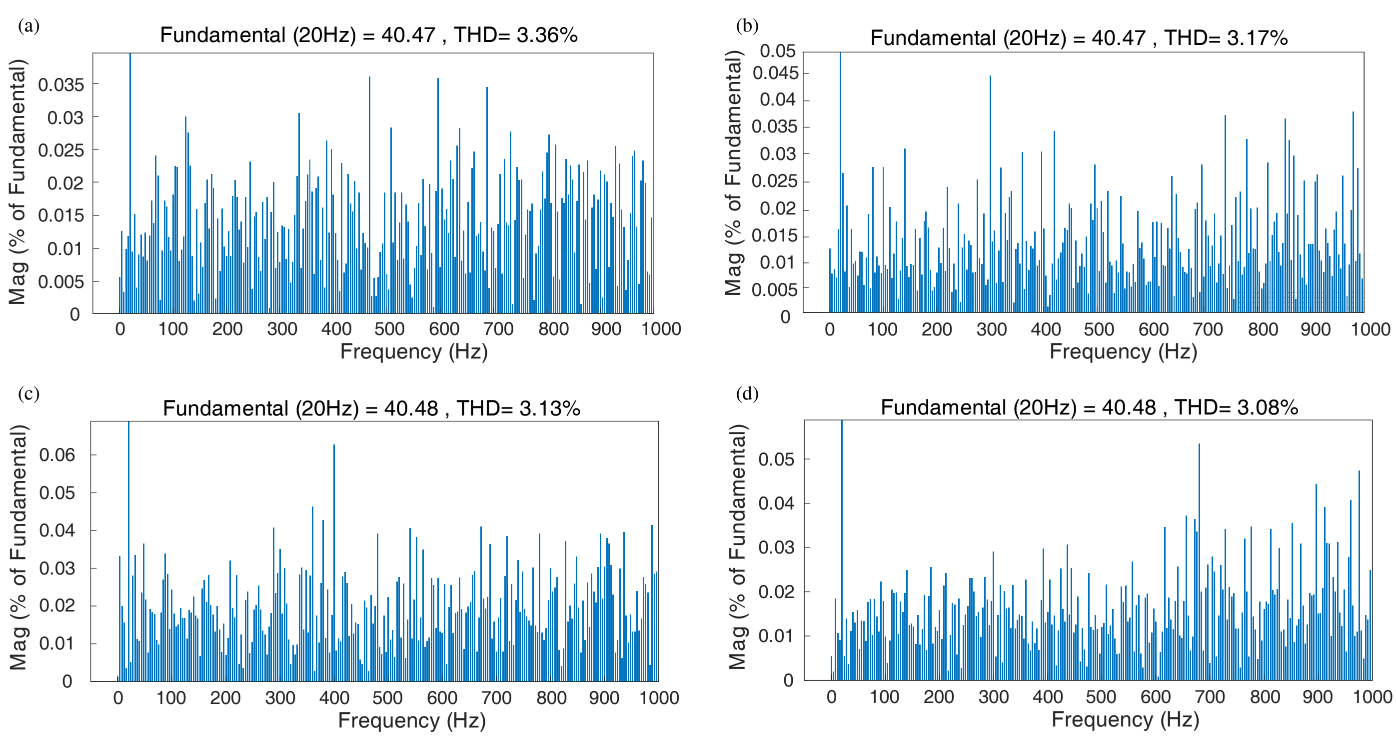

FIGURE 10. THD analysis waveforms at 1.2 s under low speed and heavy load (a) FITSMS + ESMRL, (b) ADRC (c) NFITSMS + NVGRL + STDO, and (d) NFITSMS + NVGRL + NSTDO.

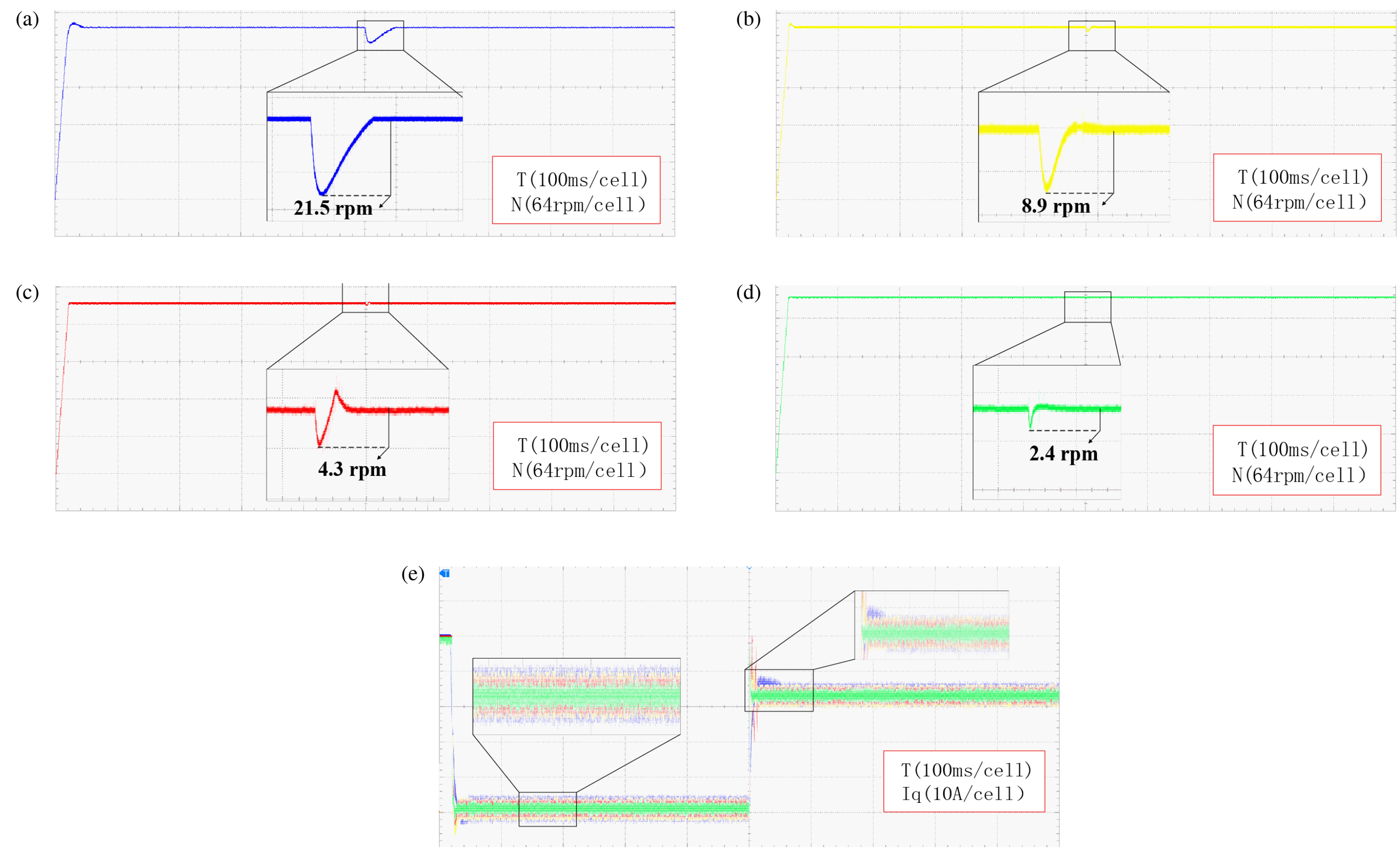

FIGURE 11. Experimental results under low-speed heavy-load condition with 1.2 J mismatch. (a) FITSMS + ESMRL, (b) ADRC, (c) NFITSMS + NVGRL + STDO, (d) NFITSMS + NVGRL + NSTDO, and (e) comparison of q-axis current.

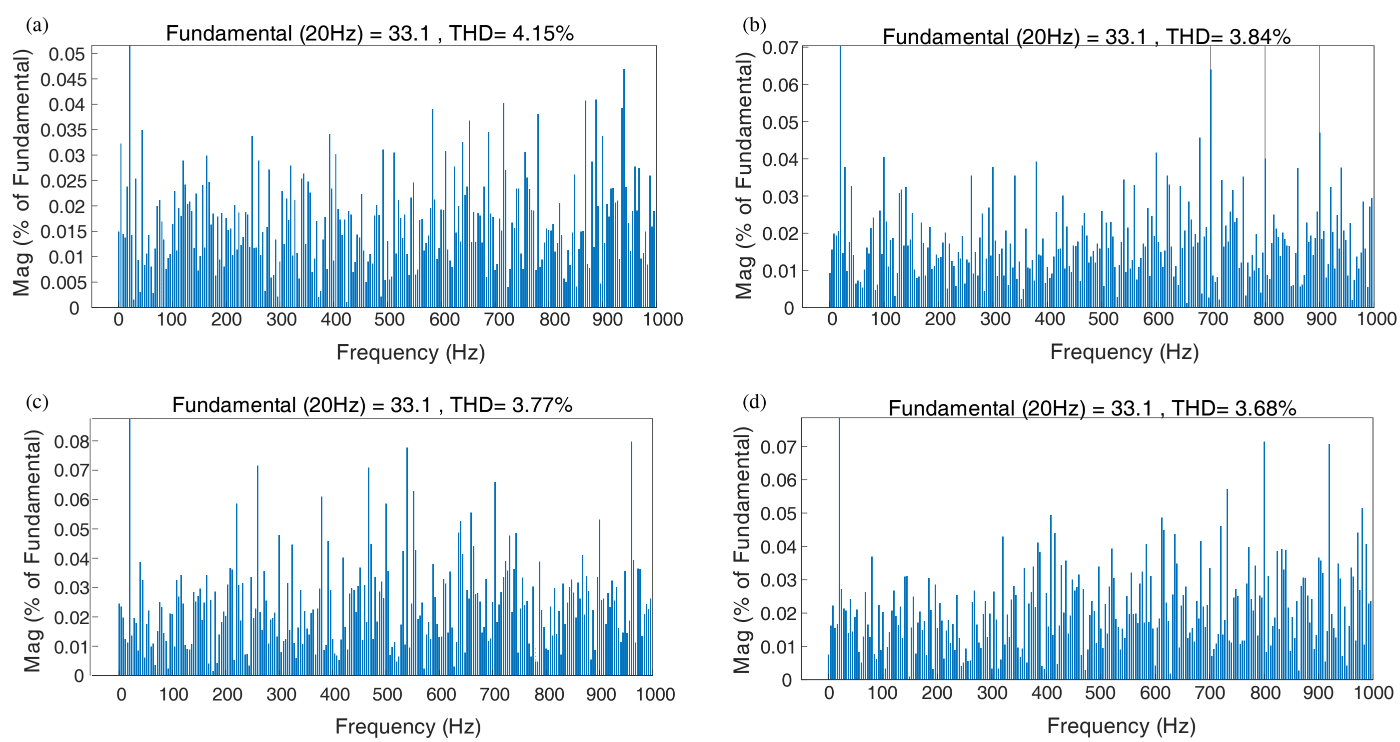

FIGURE 12. THD analysis waveforms at 0.6 s. (a) FITSMS + ESMRL, (b) ADRC (c) NFITSMS + NVGRL + STDO, and (d) NFITSMS + NVGRL + NSTDO.

TABLE 5. Performance indexes of sudden load experiment.

Symbol	Setting time (s)	Speed drop (rpm)
FITSMC	0.047	17.5
ADRC	0.04	7.5
NFITSMC + STDO	0.01	3.5
NFITSMC + NSTDO	0.008	2.3

TABLE 6. Performance indexes of rotor flux linkage variation.

Symbol	Setting time (s)	Speed drop (rpm)
FITSMC	0.016	2.4
ADRC	0.009	1.5
NFITSMC + STDO	0.006	0.3
NFITSMC + NSTDO	0.005	0.2

TABLE 7. Performance indexes of viscous friction coefficient.

Symbol	Speed RMSE	THD
FITSMC	0.01120	3.75%
ADRC	0.01075	3.25%
NFITSMC + STDO	0.09756	3.18%
NFITSMC + NSTDO	0.008802	2.92%

TABLE 8. THD and RMSE after parameter and load variation.

Symbol	Setting time (s)	Speed drop (rpm)
FITSMC	0.01	1
ADRC	0.009	0.9
NFITSMC + STDO	0.005	0.11
NFITSMC + NSTDO	0.003	0.09

TABLE 9. Performance indexes of sudden load experiment.

Symbol	Setting time (s)	Speed drop (rpm)
FITSMC	0.053	21.6
ADRC	0.02	9
NFITSMC + STDO	0.012	4.3
NFITSMC + NSTDO	0.008	2.5

cording to the control principle, the speed control performance is affected by the variation in rotational inertia J [29]. To further verify the robustness of the developed control approach, the moment of inertia was set to 1.2 times the rated value in the parameter mismatch simulation. The motor speed and q-axis current dynamic responses were analyzed under a sudden 12 N·m load impact applied at 0.5 s. As shown in Fig. 9, the conventional fast integral terminal sliding mode control is significantly affected by disturbances with a slow response speed. By contrast, the proposed control method is less sensitive to external disturbances. The THD values of the four control schemes at 0.6 s are 4.15%, 3.84%, 3.77%, and 3.68%, respectively. The proposed control algorithm reduces the harmonic content by

TABLE 10. Performance indexes of rotor flux linkage variation.

Symbol	Setting time (s)	Speed drop (rpm)
FITSMC	0.018	2.9
ADRC	0.016	1.7
NFITSMC + STDO	0.005	0.4
NFITSMC + NSTDO	0.002	0.2

TABLE 11. Performance indexes of viscous friction coefficient.

Symbol	Speed RMSE	THD
FITSMC	0.01262	3.36%
ADRC	0.0121	3.17%
NFITSMC + STDO	0.01144	3.13%
NFITSMC + NSTDO	0.009498	3.08%

TABLE 12. THD and RMSE after parameter and load variation.

Symbol	Setting time(s)	Speed drop (rpm)
FITSMC	0.005	0.3
ADRC	0.004	0.1
NFITSMC + STDO	0.002	0.04
NFITSMC + NSTDO	0.001	0.02

TABLE 13. Performance indexes of rotational inertia mismatch.

Symbol	Setting time (s)	Speed RMSE	Speed drop (rpm)	THD
FITSMC	0.055	0.01241	21.5	4.15%
ADRC	0.026	0.01173	8.9	3.84%
NFITSMC + STDO	0.016	0.01059	4.3	3.77%
NFITSMC + NSTDO	0.008	0.00995	2.4	3.68%

0.47%. The RMSE values in the time interval $0.6 < t < 1$ s were calculated to evaluate the dynamic response performance of the three methods. The results show that under a parameter mismatch of 1.2 J, the proposed method outperforms other existing strategies in reducing speed-fluctuation amplitude. The detailed numerical results are presented in Table 13.

6. CONCLUSION

This study proposes a fixed-time fast integral terminal sliding-mode speed-control strategy for SPMSM drives by combining NFITSMS, NVGRL, and NSTDO. The NVGRL accelerates convergence and suppresses chattering through fuzzy adaptive regulation. The NFITSMS guarantees fixed-time convergence and eliminates steady-state errors. The NSTDO achieves an accurate lumped disturbance estimation to enhance robustness. The Lyapunov theory proves that the closed-loop system is fixed-time stable. The experimental results show that the proposed method achieves a faster response, smaller overshoot and speed drop, lower RMSE, and reduced current THD under no-load startup, sudden load, and parameter mismatch conditions, which effectively improve the dynamic response, tracking precision, and disturbance-rejection performance of SPMSMs servo systems.

REFERENCES

[1] Cheng, Y., S. Li, and S. Li, "Time-varying sliding mode control of permanent magnet synchronous motor based on improved integral sliding mode," *Electric Machines and Control*, Vol. 28, No. 7, 160–167, 2024.

[2] Chen, L., H. Zhang, H. Wang, K. Shao, G. Wang, and A. Yazdani, "Continuous adaptive fast terminal sliding mode-based speed regulation control of PMSM drive via improved super-twisting observer," *IEEE Transactions on Industrial Electronics*, Vol. 71, No. 5, 5105–5115, May 2024.

[3] Jin, X.-Y., E. Xie, and L.-L. Zheng, "An improved I/F starting and sliding-mode sensor-less control for surface permanent synchronous motor," in *IECON 2023 — 49th Annual Conference of the IEEE Industrial Electronics Society*, 1–6, Singapore, 2023.

[4] Wu, S., Q. Zhao, and W. Tong, "Permanent magnet axial section shaping optimization surface-mounted permanent magnet synchronous motor," *CES Transactions on Electrical Machines and Systems*, Vol. 7, No. 4, 366–371, Dec. 2023.

[5] Wu, H., S. Wang, C. Gu, *et al.*, "An improved decoupling control strategy for the IPMSMS," *Transactions of China Electrotechnical Society*, Vol. 30, No. 1, 30–37, 2015.

[6] Zhu, L., G. Zhang, R. Jing, G. Bi, R. Xiang, G. Wang, and D. Xu, "Nonlinear active disturbance rejection control strategy for permanent magnet synchronous motor drives," *IEEE Transactions on Energy Conversion*, Vol. 37, No. 3, 2119–2129, Sep. 2022.

[7] Zheng, Y., Z. Cao, S. Wang, Z. Man, and R. Chuei, "Extreme learning machine-based field-oriented feedback linearization speed control of permanent magnetic synchronous motors," *Neural Computing and Applications*, Vol. 34, No. 7, 5267–5282, 2022.

[8] Li, T., X. Sun, M. Yao, D. Guo, and Y. Sun, "Improved finite control set model predictive current control for permanent magnet synchronous motor with sliding mode observer," *IEEE Transactions on Transportation Electrification*, Vol. 10, No. 1, 699–710, Mar. 2024.

[9] Zhang, W., M. Li, Y. Gao, and Y. Chen, "Periodic adaptive learning control of PMSM servo system with LuGre model-based friction compensation," *Mechanism and Machine Theory*, Vol. 167, 104561, 2022.

[10] Xu, X., L. Wang, Z. Zhang, and Z. Wu, "A novel robust control for permanent magnet synchronous motor integrating deadbeat predictive current control and sliding mode observer," *Alexandria Engineering Journal*, Vol. 130, 57–67, 2025.

[11] Fei, T., Y. Yang, C. Zheng, H. Zhang, and G. Yuan, "Adaptive neural design for permanent magnet synchronous motor with asymmetric constraints and input dead-zone," *Neurocomputing*, Vol. 640, 130294, 2025.

[12] Shi, S., L. Dai, H. Min, J. Yang, and S. Li, "Prescribed-time nonsingular terminal sliding mode control and its application in PMSM servo systems," *IEEE Transactions on Industrial Electronics*, Vol. 72, No. 3, 3072–3081, Mar. 2025.

[13] Gao, W. and J. C. Hung, "Variable structure control of nonlinear systems: A new approach," *IEEE Transactions on Industrial Electronics*, Vol. 40, No. 1, 45–55, Feb. 1993.

[14] Zhang, W. and J. Kong, "A novel fast and chattering-free speed control method for PMSM motor drive based on sliding mode control," *International Journal of Dynamics and Control*, Vol. 12, No. 9, 3332–3338, 2024.

[15] Park, J., H. Ahn, M. Hu, H. Kwon, and K. You, "Enhanced composite adaptive sliding mode reaching law for speed regulation in SPMSM," *Results in Engineering*, Vol. 25, 104567, 2025.

[16] Dong, H., Q. Du, K. Liu, *et al.*, "Dynamic performance optimization of permanent magnet synchronous motor based on new reaching law," *Packaging Engineering*, Vol. 44, No. 5, 163–170, 2023.

[17] Huang, J., Y. Wang, Y. Yang, *et al.*, "Deadbeat predictive control for PMSM based on improved sliding mode observer," *Journal of Power Supply*, 2025 (in Chinese).

[18] Ma, X., L. Zhang, Y. Xu, and J. Bai, "Model-free control of permanent magnet synchronous motors with improved terminal sliding mode based on a modified exponential reaching law," *Control Engineering Practice*, Vol. 166, 106630, 2026.

[19] Wu, S., X. Su, and K. Wang, "Time-dependent global nonsingular fixed-time terminal sliding mode control-based speed tracking of permanent magnet synchronous motor," *IEEE Access*, Vol. 8, 186 408–186 420, 2020.

[20] Chen, Y., J. Liu, and Z. Yao, "PMSM sliding mode control based on disturbance observer and new non-singular fast terminal," *Modular Machine Tool & Automatic Manufacturing Technique*, No. 3, 84–87, 2022.

[21] Li, T., Y. Zhao, and L. Hou, "Adaptive sliding mode control with disturbance observer for speed regulation system of permanent magnet synchronous motor," *IEEE Access*, Vol. 11, 17 021–17 030, 2023.

[22] Kong, D., H. Cai, and W. Zeng, "A predefined time fast terminal sliding mode predictive speed control for PMSM drives," *IEEE Transactions on Power Electronics*, Vol. 40, No. 7, 9068–9079, Jul. 2025.

[23] Zhang, X., L. Sun, K. Zhao, and L. Sun, "Nonlinear speed control for PMSM system using sliding-mode control and disturbance compensation techniques," *IEEE Transactions on Power Electronics*, Vol. 28, No. 3, 1358–1365, Mar. 2013.

[24] Zhang, L., R. Tao, Z.-X. Zhang, Y.-R. Chien, and J. Bai, "PMSM non-singular fast terminal sliding mode control with disturbance compensation," *Information Sciences*, Vol. 642, 119040, 2023.

[25] Shi, S., Y. Wang, and S. Mai, "Research on speed control of PMSM based on a new sliding mode reaching law of fast integral terminal sliding mode control with iterative-based high-gain disturbance observer," *IEEE Transactions on Industry Applications*, Vol. 61, No. 3, 4352–4363, May-Jun. 2025.

[26] Liang, T., X. Li, P. Wang, and H. Mao, "Sliding mode control of permanent magnet synchronous motor based on hierarchical nonsingular terminal and super-twisting sliding mode disturbance observer," *Journal of Ordnance Equipment Engineering*, Vol. 46, No. 2, 196–203, 2025.

[27] Polyakov, A., "Nonlinear feedback design for fixed-time stabilization of linear control systems," *IEEE Transactions on Automatic Control*, Vol. 57, No. 8, 2106–2110, Aug. 2012.

[28] Chen, L., H. Zhang, H. Wang, K. Shao, G. Wang, and A. Yazdani, "Continuous adaptive fast terminal sliding mode-based speed regulation control of PMSM drive via improved super-twisting observer," *IEEE Transactions on Industrial Electronics*, Vol. 71, No. 5, 5105–5115, May 2024.

[29] Zhang, Z. and X. Liu, "An improved super-twisting sliding mode single-loop control with current-constraint for PMSM based on two-time scale disturbance observer," *IEEE Transactions on Transportation Electrification*, Vol. 10, No. 3, 5389–5399, Sep. 2024.